Supplementary Information for

De-templated crystallization in 2D Perovskites for Enhanced

Photovoltaic Efficiency

Authors: Fang Zeng[1,2], Zhenhuang Su[4], Weiyu Kong[2], Feng Li[1], Yuhang Liang[1,3], Xingmo Zhang[1,3], Tao Wang[2], Lin Zhang[2], Yuze Lvtao[1], Runkai Liu[1], Xingyu Gao[4], Jun Huang[3], Xudong Yang[2], Rongkun Zheng[1]

Affiliations:

[1] School of Physics, The University of Sydney, Sydney NSW 2006, Australia.

[2] State Key Laboratory of Metal Matrix Composites, Shanghai Jiao Tong University, Shanghai 200240, China.

[3] School of Chemical and Biomolecular Engineering. The University of Sydney, Sydney NSW 2006, Australia.

[4] Shanghai Synchrotron Facility (SSRF), Shanghai Advanced Research Institute, Chinese Academy of Sciences, Shanghai 201204, China.

This file includes:

Methods.

Supplementary Figures 1-24.

Supplementary Tables 1-11.

Supplementary References.

Methods

Materials

Formamidinium iodide (FAI, 99.99%), lead iodide (PbI$_2$, 99.99%), and organic spacers including Hexylamine Hydroiodide (HAI), phenylethylammonium iodide (PEAI), and thiourea (TU) were purchased from TCI. Methylammonium chloride (MACl, 98%), and 2,2',7,7'-Tetrakis [N, N-di(4-methoxyphenyl) amino]-9,9'-spirobifluorene (Spiro-OMeTAD) was purchased from Borun New Material Corp. Bis-(trifluoromethane) sulfonimide lithium salt (Li-TFSI) and 4-tert-butyl-pyridine (tBP) were purchased from Sigma-Aldrich. A colloidal dispersion of tin (IV) oxide (SnO2, 15%) was purchased from Alfa Aesar. All solvents, including N, N'-dimethylformamide (DMF, 99.8%, anhydrous), dimethyl sulfoxide (DMSO,99.8%, anhydrous), and chlorobenzene CB (>99.8%) were sourced from Sigma-Aldrich. The Indium-tin Oxide (ITO) glass and Fluorine-doped Tin Oxide (FTO) glass were purchased from Advanced Election Technology Co., Ltd.

Perovskite precursor solution

For the conventional two-step method (TTSD), the PbI$_2$ (1.0 mol) was dissolved in a solvent mixture of DMF and DMSO solution, while the FAI, HAI, and MACl (6 mg/ml) were dissolved in the IPA solution. The modified TTSD method with TU in the first step was defined in ATSD. The modified TTSD with HAI preponed to the first step was defined in STSD. In the SATD spin-coating method, a mixture containing HAI, FAI, and PbI$_2$ at the same stoichiometric ratio of n=4, HAI and PbI$_2$ were prepared, and TU added to the PbI$_2$ precursors at concentrations ratio of PbI$_2$: TU=1:0.5, 1:1 and 1:2, and 1:2 in the DMF and DMSO solutions (volume ratio 9:1), respectively. The FAI and MACl (6 mg/ml) were dissolved in the IPA solution. PEAI and ThDMA-based 2D FA perovskite films were prepared by dissolving these compounds along with TU and PbI$_2$ in mixed solvents of DMF and DMSO (volume ratio 9:1). FAI and MACl (6 mg/ml) were dissolved in IPA solution, maintaining a stoichiometric ratio of 2:3:4 (n=4). HA-based 2D FA perovskite films with different layers (n=2 and n=3) were prepared by a stoichiometric ratio of 2:1:2 (n=2), and 2:2:3 (n=3), by dissolving HAI, TU, and PbI$_2$ in mixed solvents of DMF and DMSO. Similarly, FAI and MACl were dissolved in IPA solution, respectively.

Device fabrications

The production of perovskite solar cells commenced with the preparation of ITO glass with the pre-patterned substrates. These substrates underwent a cleaning regimen, involving ultrasonic baths of detergent, deionized water, ethanol, and acetone, followed by a UV Ozone cleaning process, with each stage lasting for 15 minutes. Subsequently, a SnO$_2$ colloidal dispersion (diluted to 15% with deionized water at a ratio of 1:5) was coated onto the substrates at a spin speed of 3000 rpm for 30 seconds and underwent an annealing process at 150 °C for 30 minutes. The creation of one-step perovskite films involved depositing a precursor solution onto the substrates at a spin speed of 4000 rpm for 30 seconds, with an anti-solvent of 300 µL chlorobenzene introduced 15

seconds before the end. The two-step method involved depositing a metal halide precursor solution onto the substrates at a spin speed of 3000 rpm for 30 seconds in the first step and spin-coating IPA solution of organic cations at a spin speed of 5000 rpm for 30 seconds in the second step. These films were then subjected to thermal annealing at 150 °C on a hotplate for 30 minutes to finalize their structure. Following this, a Spiro-OMeTAD solution was spin-coated over the perovskite layer as a hole-transport material at 3000 rpm for 30 seconds. This solution was prepared by dissolving 73 mg of Spiro-OMeTAD in 1 ml of chlorobenzene, with the addition of 17.5 µL Li-TFSI (520 mg/ml in acetonitrile) and 28.8 µL of 4-tBP as dopants. The fabrication concluded with the thermal evaporation of 60-nm thick gold electrodes, ensuring a robust electrical connection for the cells.

Characterization of perovskite films

UV-Vis absorption measurements of perovskite films were conducted using a Shimadzu UV 2450 spectrometer. X-ray diffraction (XRD) patterns were obtained using Rigaku Dmax 2600 diffractometer via using Cu $K\alpha$ radiation with a Nickel filter. X-ray photoelectron spectroscopy (XPS) was performed on the AXIS Ultra DLD (Kratos) spectrometer. Grazing incidence wide-angle X-ray scattering (GIWAXS) data were collected at beamline BL14B1 of the Shanghai Synchrotron Radiation Facility (SSRF) using X-ray with a wavelength of 1.2398 Å. Transmission Electron Microscopic (TEM) was used FEI Themis-Z Double-corrected 60-300Kv S/TEM. The perovskite films were scratched off from the substrate and dispersed in toluene by sonication for 10 min, followed by being dropped on a Cu grid for characterization. Photoluminescence (PL) Measurements were performed using an FLS1000 spectrometer (Edinburgh Instruments) with 470 nm excitation wavelength, and the PL mapping was collected on a Leica TCS SP8 STED 3X super-resolution system. Time-resolved photoluminescence spectra (TRPL) were obtained by using the same spectrometer as that for the steady PL experiments. Both the top-view and cross-sectional scanning electron microscopy (SEM) measurements for perovskite samples were conducted using Tescan Maia3 Gmu (model 2016). Kelvin probe force microscopy (KPFM) measurement data were obtained using a Dimension Fast Scan Bio Atomic Force Microscope. Elemental Analysis (EA) was conducted on a Thermo Fisher Flash Smart elemental analyzer.
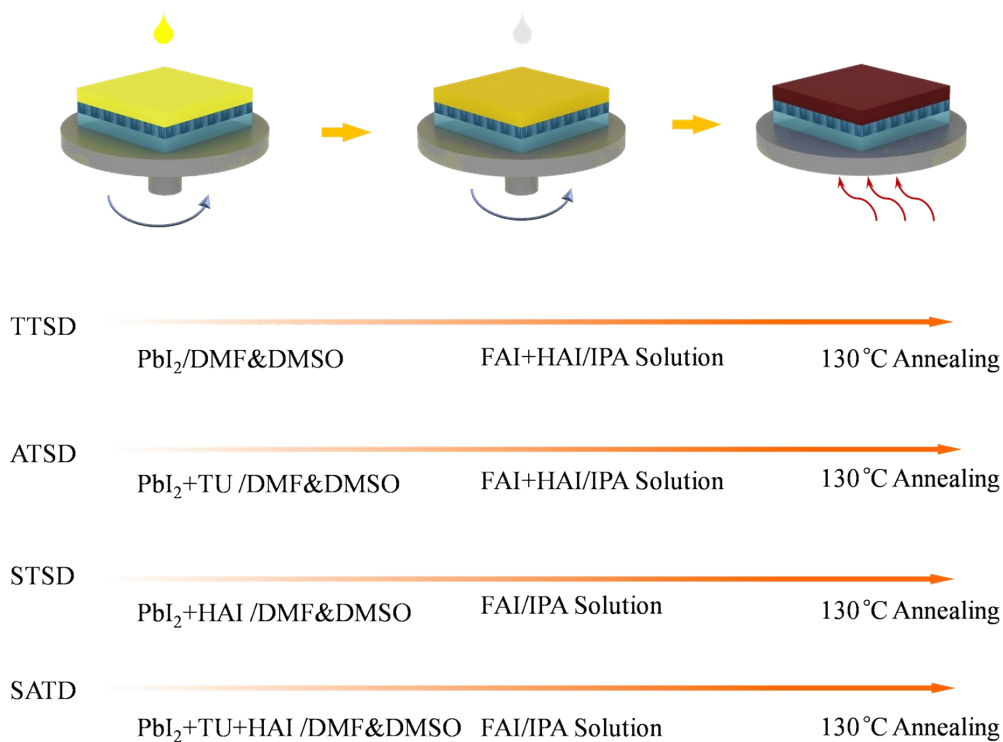
Device characterization and Stability measurement

Current density-voltage (J-V) curves were obtained using a Keithley 2400 source-meter under AM 1.5G 1-sun illumination from a 3A simulator (Newport, Oriel® Sol3A™, 94023A). The system was calibrated using a standard silicon reference cell (Newport, Newport Oriel 91150-KG5). Measurements were conducted on devices with active areas of 0.08 cm^2 and 1.02 cm^2. Incident photo-to-electron conversion efficiency (IPCE) spectra measurements were characterized using monochromatic incident light of 1×10^{16} photons cm^{-2} with the alternating current mode. Accelerated aging tests were conducted at 25° and a relative humidity (RH) of 50-60%. Heat stability was assessed by placing non-encapsulated PSCs on a hotplate within an aging box maintained at

85°C, and PCE evolution was monitored through periodic *J-V* measurements. Long-term operational stability was tested on the solar cell light resistance testing system of Model BIR-50. Long-term operational stability was evaluated using a Model BIR-50 solar cell light resistance testing system. The stability of the unencapsulated photovoltaic devices was measured under continuous one-sun illumination in an N_2-filled glove box. For all stability tests, the hole transport layer was modified by ion-exchanged PTAA, details of which are described in previous work[1].

Computational method

All the first-principles density functional theory (DFT) calculations [2] were performed as implemented in the Vienna ab initio simulation package (VASP)[3]. The DFT-D3 scheme of Grimme was adopted for describing van der Waals (vdW) interactions[4]. Projector-augmented wave (PAW) pseudopotentials were used to model the valence states and the interactions between core and valence electrons[5]. The Perdew-Burke-Ernzerhof (PBE)[6] form of the generalized gradient approximation (GGA) was employed for describing the exchange and correlation function, and the spin-orbit coupling (SOC) was included. Plane-wave functions were expanded with an energy cutoff of 500 eV and the Brillouin zone was sampled using a Monkhorst–Pack sampling of 4*4*4 k-point grid. All the geometries were fully relaxed until the forces on each atom were less than 0.01 eV/Å. The system of interest is isolated molecules. The binding energies of the compound (E_b) relative to its isolated molecules were calculated using the following method, where $E_b = E_{total} - \Sigma E_{isolated\ molecules}$, Where E_{total} and $\Sigma E_{isolated\ molecules}$ is the total energy of the compound and individual isolated molecules. Regarding the calculation and mapping of ESP, we used Gaussian for calculating the ESP of the molecular structure. The stabled wavefunctions were calculated using Perdew-Burke-Ernzerhof (PBE0) hybrid functional, with mixed pseudopotentials and basis sets (6-311G* for light elements and SDD-MWB for Pb, I, respectively). The results are corrected with D3 version of Grimme's dispersion with Becke-Johnson damping. After that, the electrostatic potential was then mapped onto the van der Waals surface of the molecule to visualize the charge distribution.

| TTSD | PbI$_2$/DMF&DMSO | FAI+HAI/IPA Solution | 130°C Annealing |
ATSD	PbI$_2$+TU /DMF&DMSO	FAI+HAI/IPA Solution	130°C Annealing
STSD	PbI$_2$+HAI /DMF&DMSO	FAI/IPA Solution	130°C Annealing
SATD	PbI$_2$+TU+HAI /DMF&DMSO	FAI/IPA Solution	130°C Annealing

Supplementary Fig. 1. Fabrication flowchart of 2D perovskite films based on different two-step deposition methods. **a)** traditional two-step sequential deposition method as defined in TTSD method (PbI$_2$; FAI+HAI), **b)** a modified additive-assisted two-step sequential deposition as defined in ATSD method (PbI$_2$+TU; FAI+HAI). **c)** a modified spacer-cation-preponed two-step sequential deposition as defined in STSD method (PbI$_2$+HAI; FAI+HAI), **d)** Target spacer-cation-preponed additive-stabilized two-step deposition (SATD) method (PbI$_2$+TU+HAI; FAI), respectively.
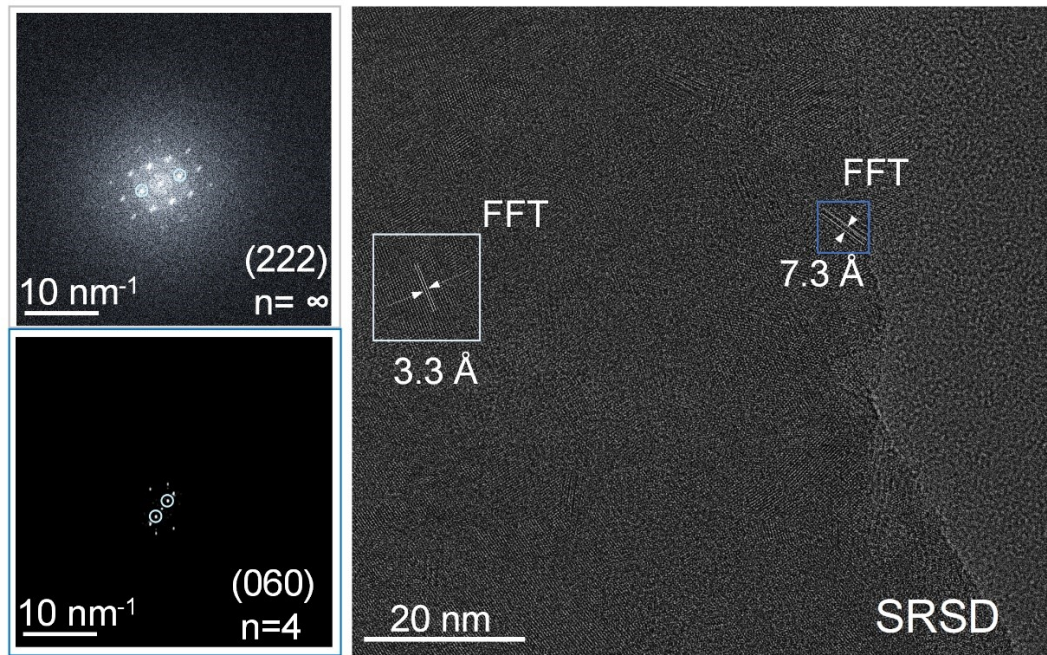
Supplementary Fig. 2. High-Resolution Transmission Electron Microscopy (HRTEM) images and corresponding Fast Fourier Transform (FFT) analysis of 2D perovskite film produced using the SATD strategy.
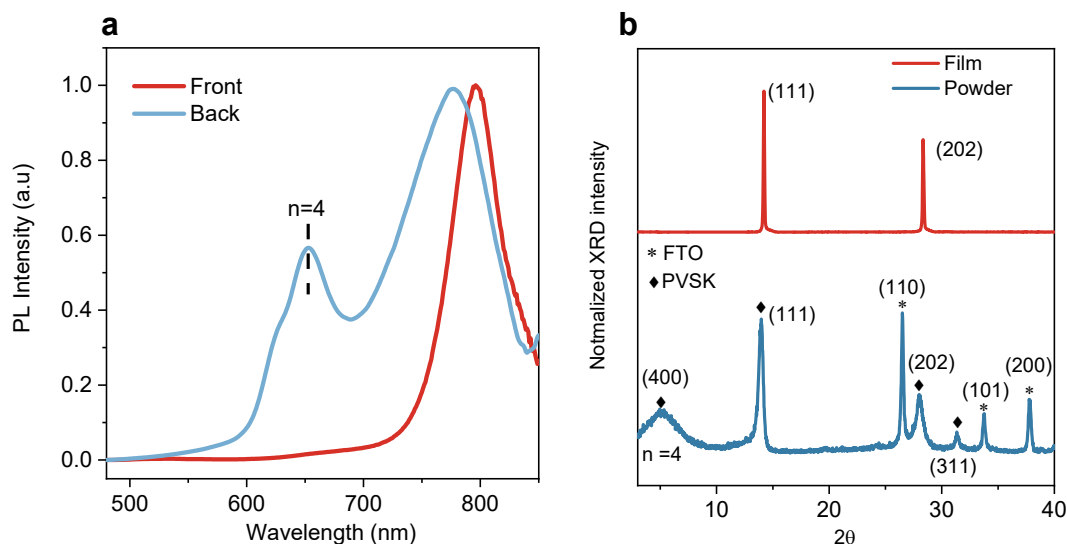
Supplementary Fig. 3. (a) PL spectra of the resulted SATD film excited from the front side (film side) and back side (glass side). (b) XRD patterns of the resulted 2D perovskite films and powders, respectively. PL measurements were conducted from both the front and back sides of the film. The front-side PL spectrum predominantly exhibits emission from the 3D-like perovskite phase, whereas the back-side spectrum reveals, in addition to the bulk phase signals, a distinct emission around 650 nm range corresponding to the 2D phase (n=4). This observation indicates that 2D perovskite is primarily distributed near the back of the film, close to the substrate, while the 3D phase is more concentrated on the surface. This is consistent with our crystallization theory, where the 3D-like phase guides the crystallization of 2D perovskite after the deposition of FAI. The XRD for the resulted SATD film revealed strong out-of-plane diffraction of the perovskite, indicative of vertical orientation of 2D micro-crystals. To confirm the 2D phase, we performed XRD for perovskite powders that directly scraped from the substates, eliminated the orientation effect. The results clearly shown (400) diffraction peak of the 2D $HA_2FA_3Pb_4I_{13}$ perovskite. This further confirms the presence of the 2D phase within the film and demonstrates that our SATD strategy effectively promotes vertical orientation.
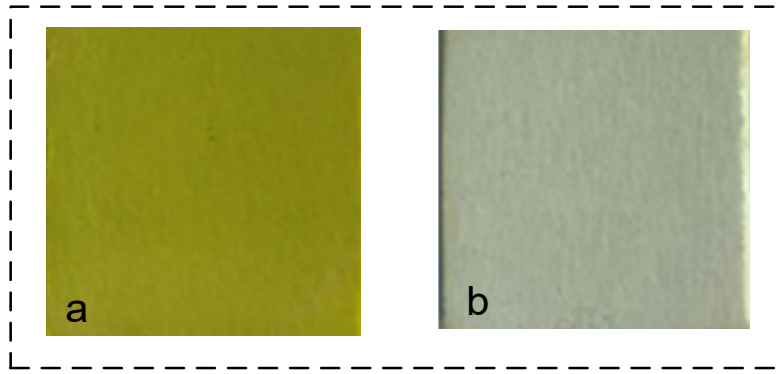
Supplementary Fig. 4 Optical photo of wet perovskite film after the first deposition step using **a)** TTSD method and **b)** target SATD method, the SATD sample exhibited nearly colorless compared to the yellow PbI$_2$ films.
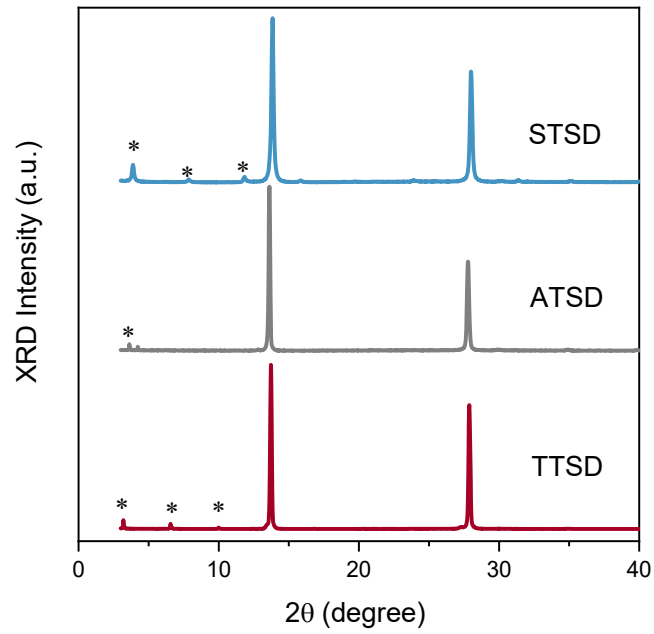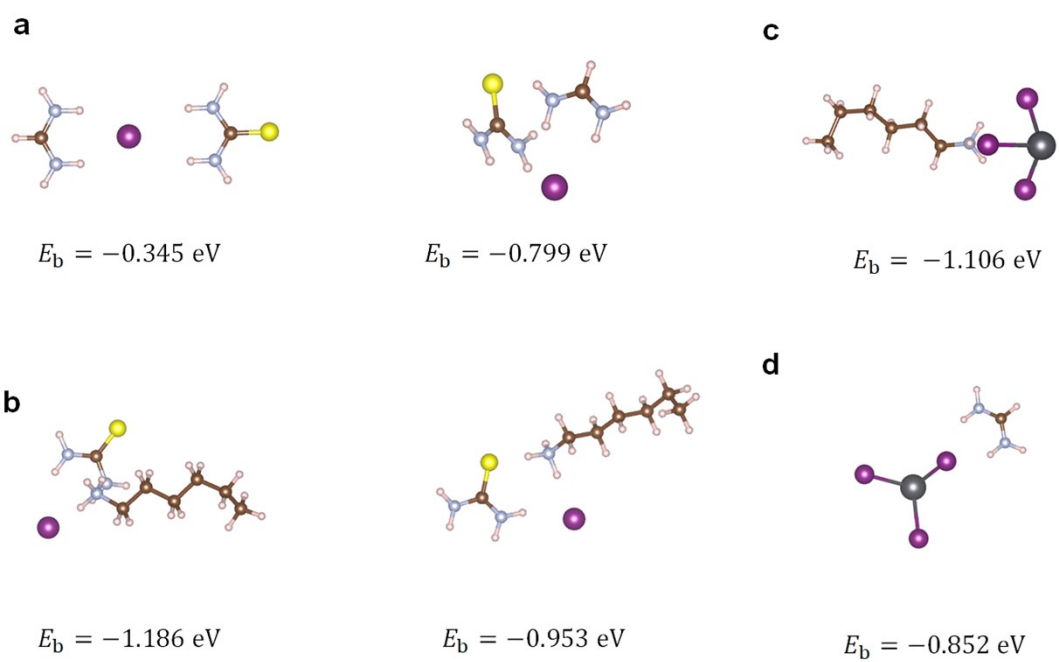
Supplementary Fig. 5. XRD patterns of 2D FA-based perovskite films after annealing, with different deposition methods as shown in Supplementary Fig. 1 (the asterisk * represents the 0*k*0 crystal plane).
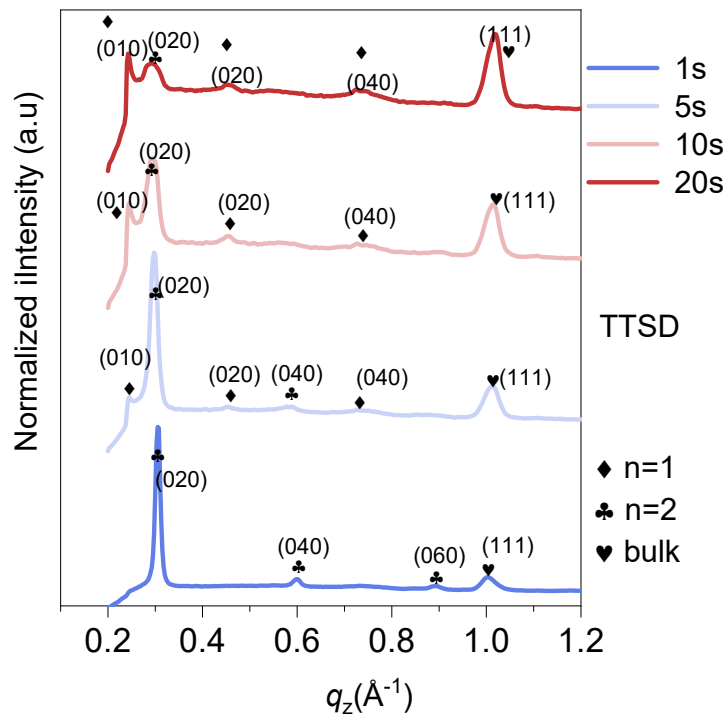
Supplementary Fig. 6. Integrated diffraction intensity along the out-of-plane direction of GIWAXS patterns for the TTSD 2D perovskite films. The calibration of diffraction peaks is based on the literature [7-9].
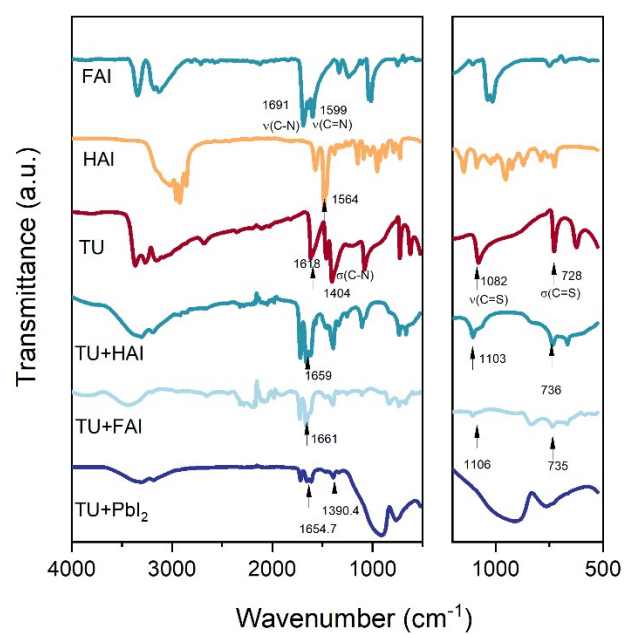
Supplementary Fig. 7. FTIR spectra of the TU and that interacted with different perovskite components (FAI, HAI, and PbI$_2$), respectively.

a

$E_b = -0.345$ eV

$E_b = -0.799$ eV

c

$E_b = -1.106$ eV

b

$E_b = -1.186$ eV

$E_b = -0.953$ eV

d

$E_b = -0.852$ eV

Supplementary Fig. 8. Calculated possible molecular configurations between (a) FAI and TU, **b)** HAI and TU, **c)** PbI_2 and HAI, **d)** FAI and PbI_2, respectively, the binding energy E_b was also calculated based on DFT.
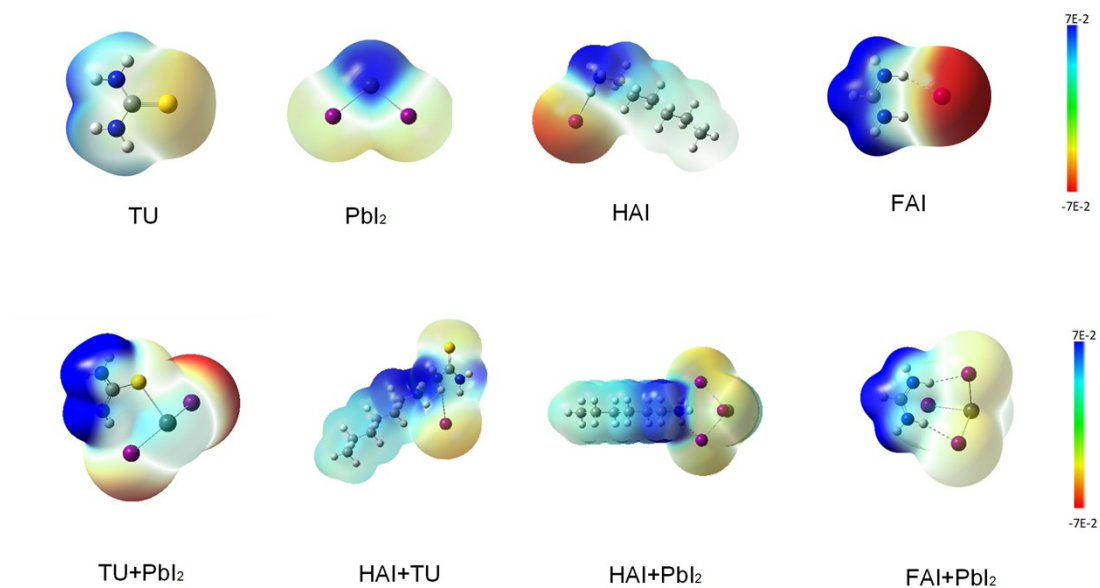
Supplementary Fig. 9. Molecular structures and calculated electrostatic potential (ESP) mapping profiles of TU, PbI$_2$, HAI, and FAI, respectively, and the interacted complexes between these components. The ESP color bar ranges from -0.07 to 0.07 for a clear comparison.
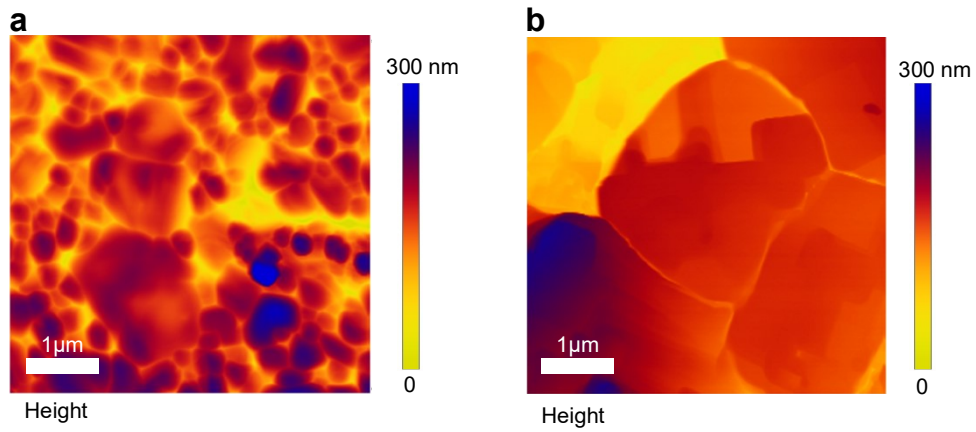
Supplementary Fig. 10. (a-b) AFM images of 2D perovskite film using TTSD and SATD strategy, respectively.

a PbI₂:Tu =1:0.5
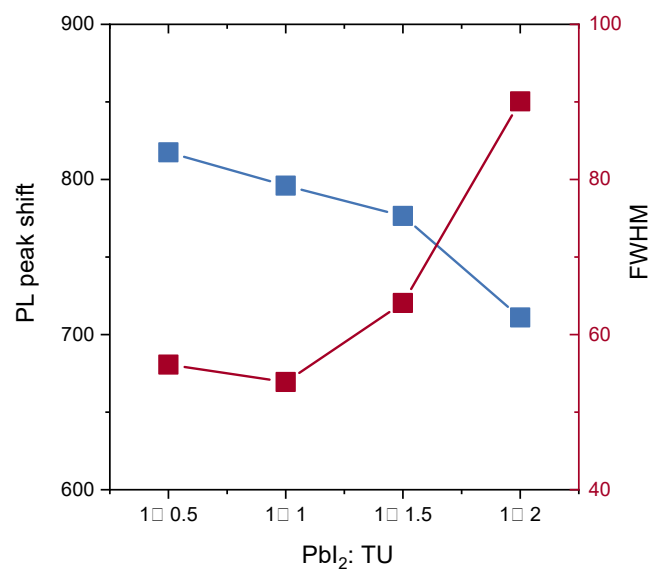
b PbI₂:Tu =1:1

c PbI₂:Tu =1:2
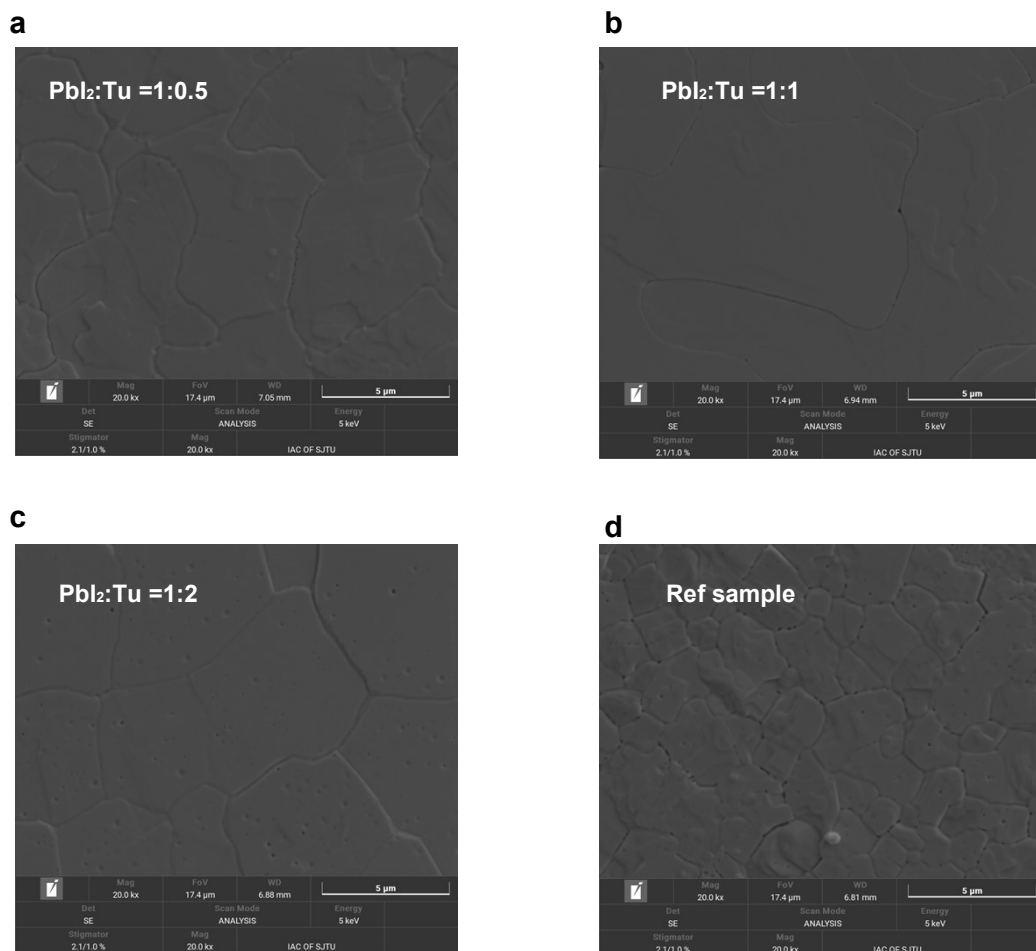
d Ref sample

Supplementary Fig. 11. (a) Top-view scanning electron microscopy (SEM) images of TU-treated 2D FA perovskite films with different incorporation ratios: (a) PbI₂: TU: =1:0,5; (b) PbI₂: TU =1:1; (c)PbI₂: TU =1:2, and (d) Ref sample, respectively.
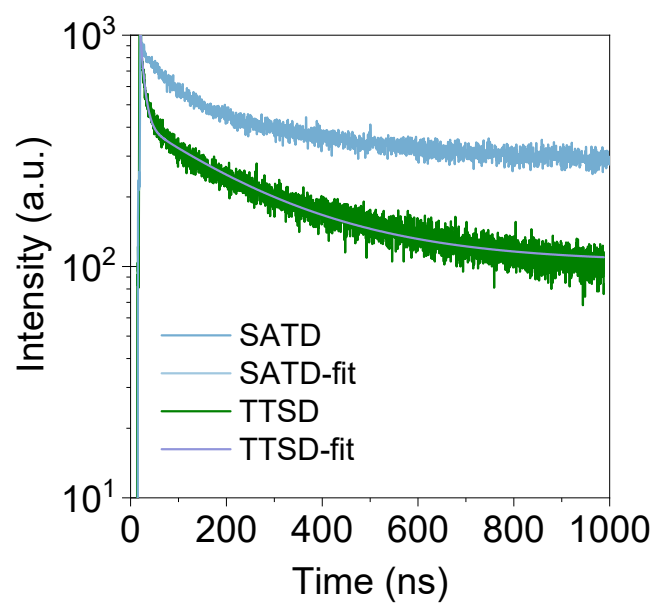
Supplementary Fig. 12. TRPL of the TTSD and the SATD perovskite films and carrier lifetimes are summarized in **Supplementary Table 1.** The TRPL decays were fitted using the equation: $y=A_1\exp(-t/\tau_1) +A_2\exp(-t/\tau_2)$, where A_1 and A_2 are the amplitudes, τ_1 and τ_2 are the PL decay times.

Supplementary Fig. 13. Corresponding PL peak shift (excited from front side) and FWHM variation of 2D FA perovskite films with different TU incorporated ratios, from PbI_2: TU: =1:0.5 to PbI_2: TU =1:2, respectively.
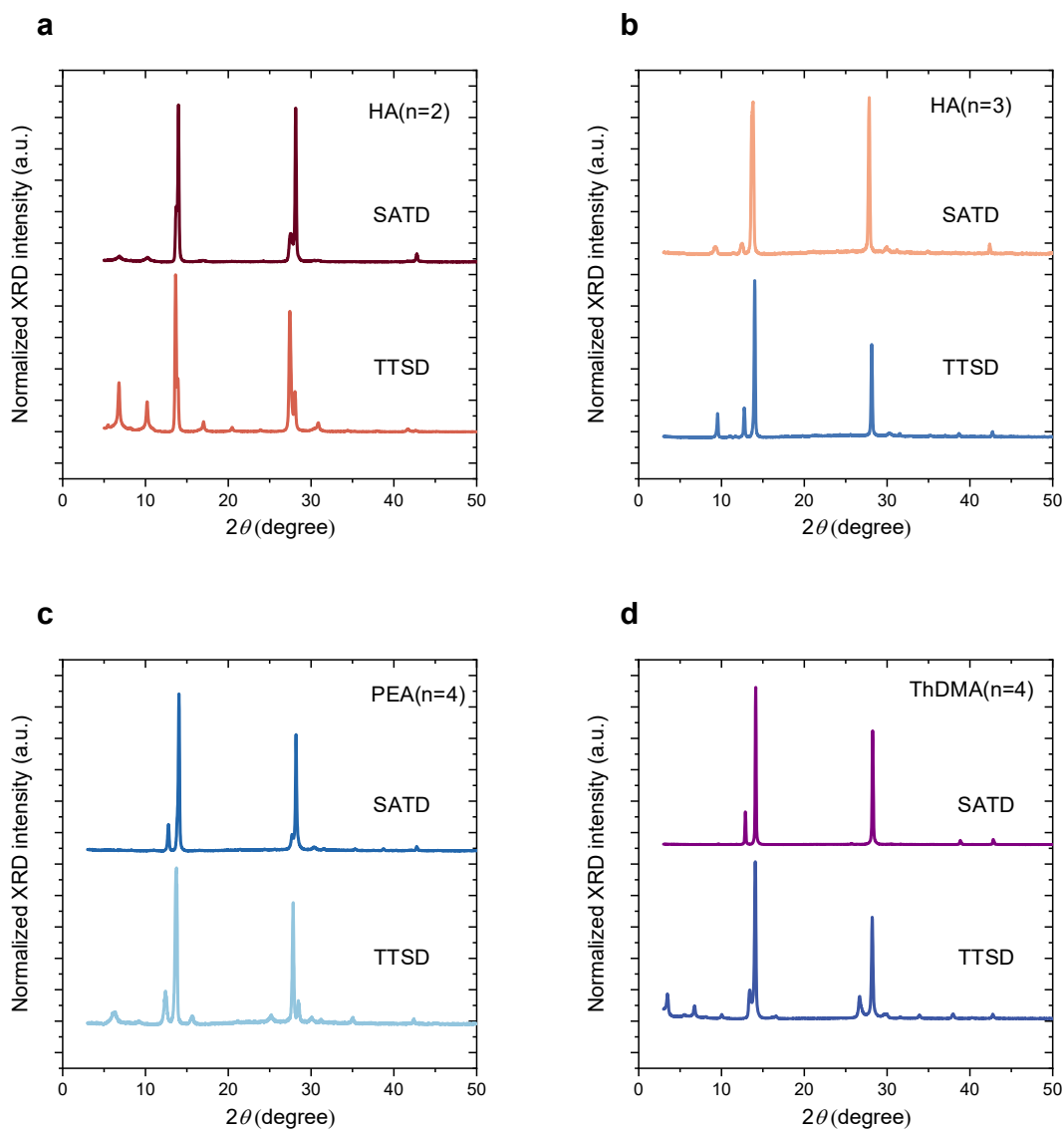
Supplementary Fig. 14. XRD patterns of 2D FA perovskite films treated by TTSD and SATD strategy, respectively. **a)** HA ($n = 2$), **b)** HA ($n = 3$), **c)** PEA ($n = 4$), and **d)** ThDMA ($n = 4$).
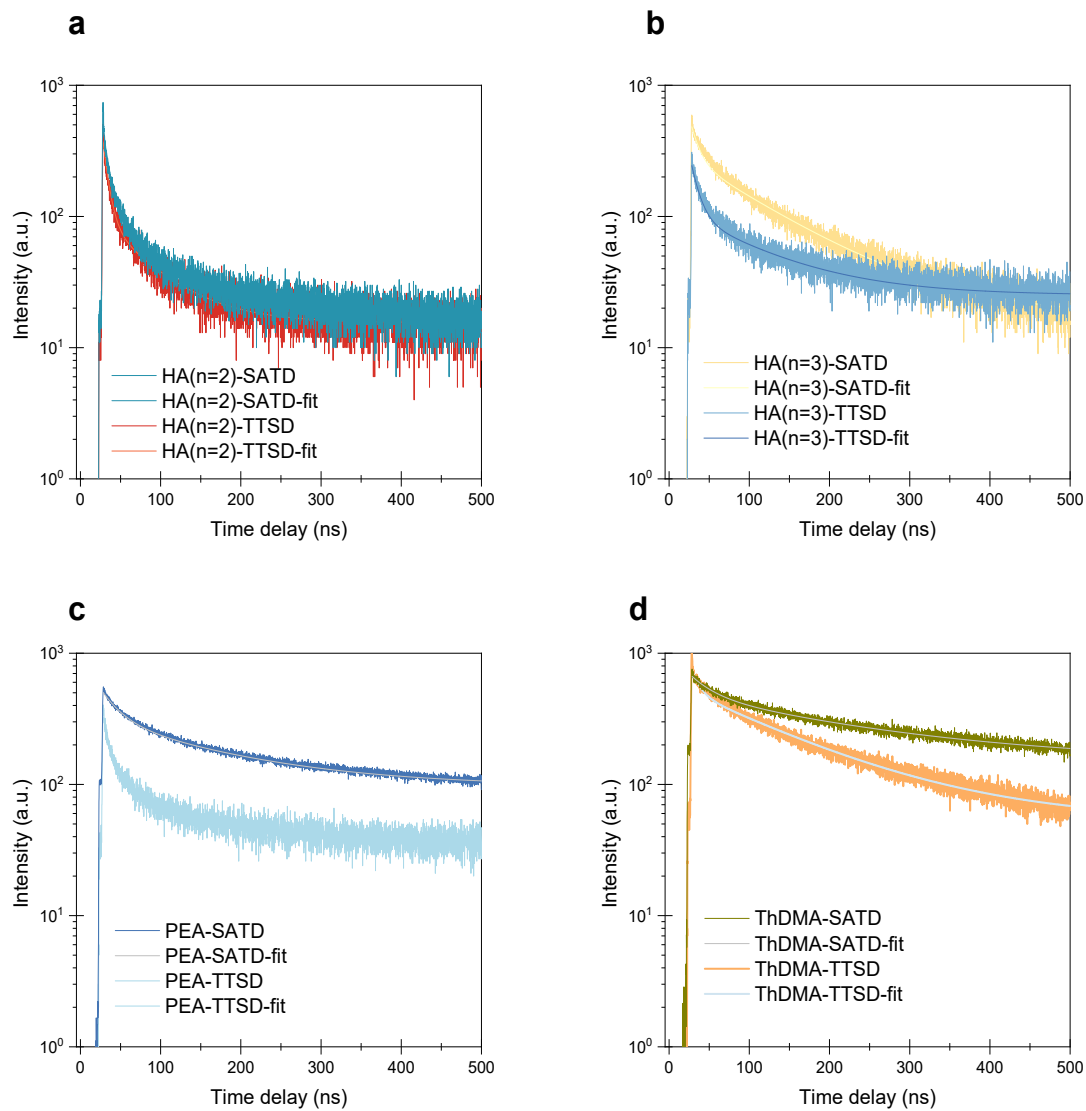
Supplementary Fig. 15. Comparison of TRPL of 2D FA perovskite films treated by TTSD and SATD strategy, respectively. **a)** HA (*n* = 2), and **b)** HA (*n* = 3), **c)** PEA (*n* = 4), **d)** ThDMA (*n* = 4). The charge carrier lifetime is summarized in **Supplementary Table 2.**
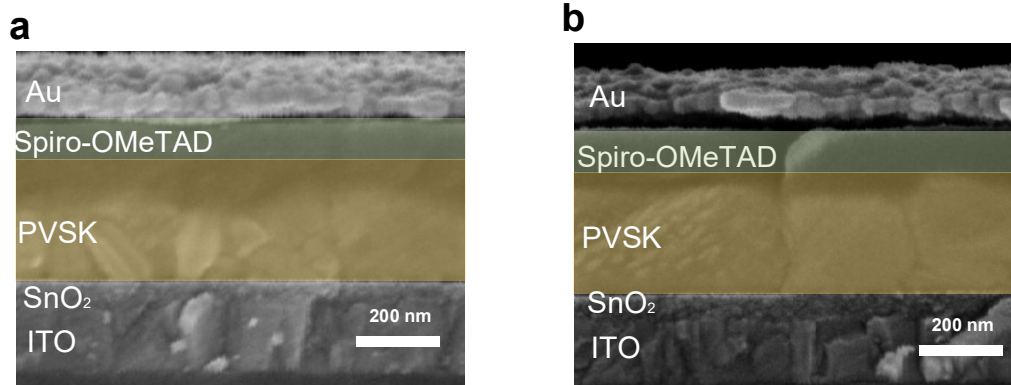
Supplementary Fig. 16. Cross-section scanning electron microscopy (SEM) image of PSC fabricated based on **a)** the TTSD method and **b)** the target (SATD) method, respectively.
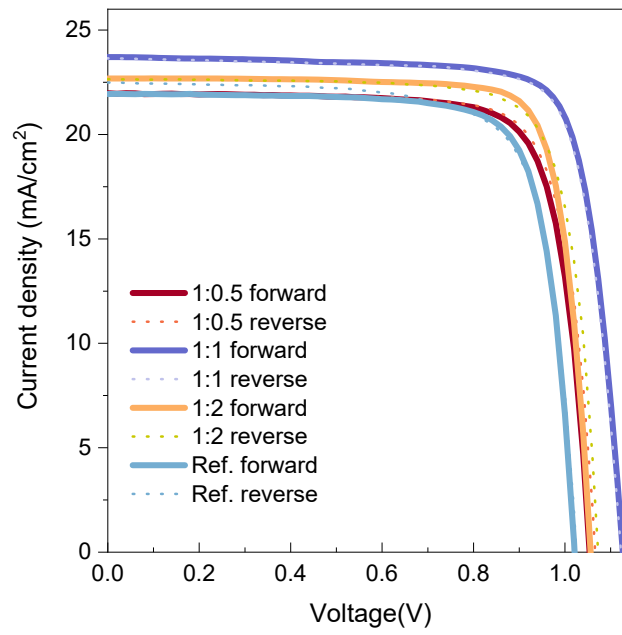
Supplementary Fig. 17 *J–V* curves (under forward and reverse scanning direction) of TU-treated 2D FA perovskite films with different incorporation ratios, control sample, PbI_2: TU: =1:0.5, PbI_2: TU =1:1, and PbI_2: TU =1:2, respectively. The main parameters of the best devices are summarized in **Supplementary Table 4**.
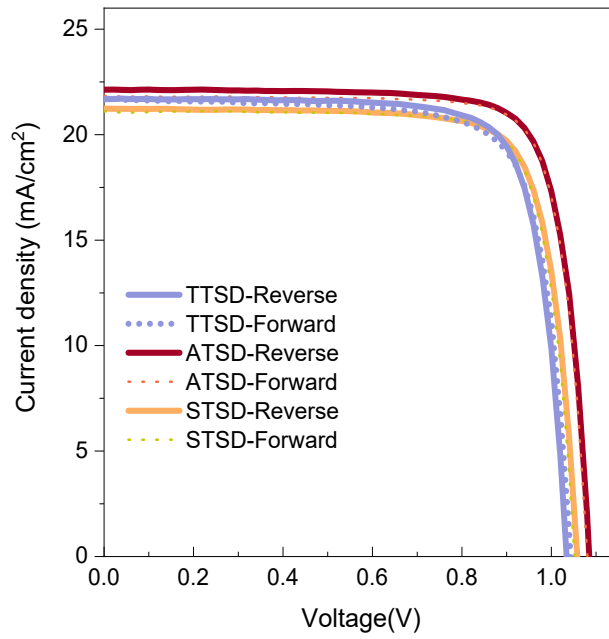
Supplementary Fig. 18. *J–V* curves (under forward and reverse scanning direction) of the optimized FA-based 2D PSCs based on TTSD, ATSD, and STSD methods, respectively. The main parameters of the best devices are summarized in **Supplementary Table 5**.
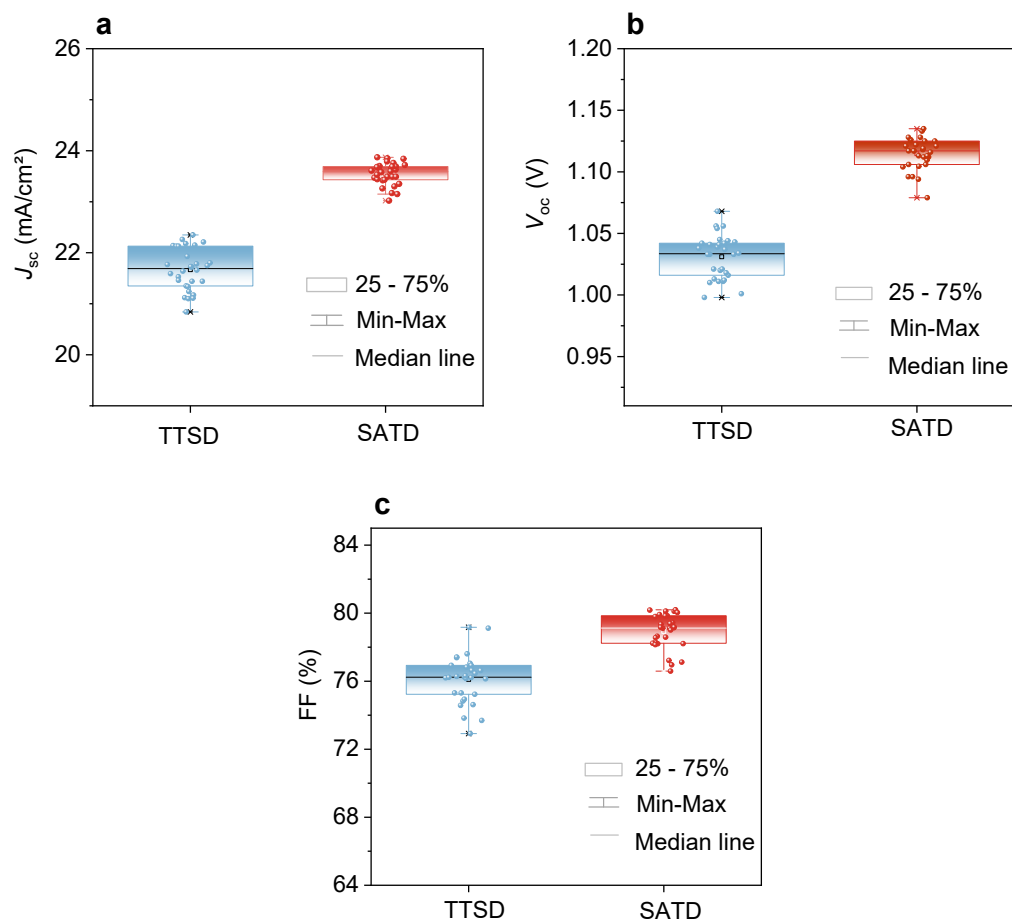
Supplementary Fig. 19. Statistical distributions of J_{sc}, V_{oc}, and FF for both TTSD and SATD based 2D perovskite solar cells, and the corresponding parameters of each device are summarized in **Supplementary Table 7.**
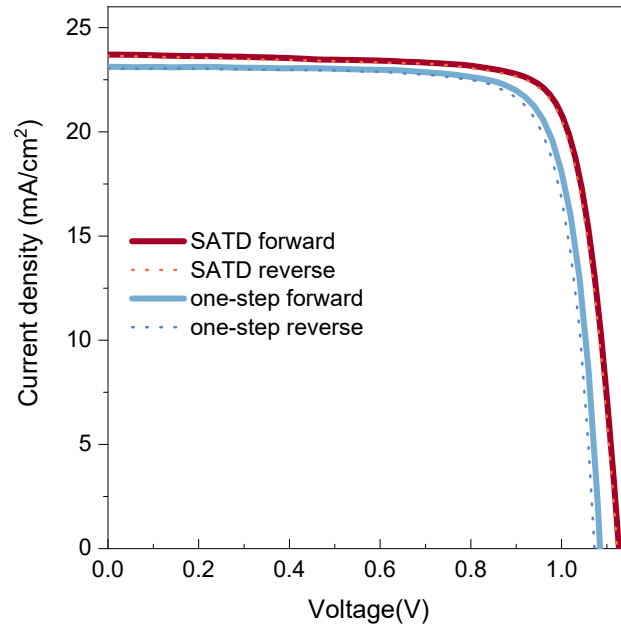
Supplementary Fig. 20. *J–V* curves (under forward and reverse scanning direction) of 2D FA-based PSCs based on SATD strategy and traditional one-step method of adding TU, respectively. The main parameters of the best devices are summarized in **Supplementary Table 8**.
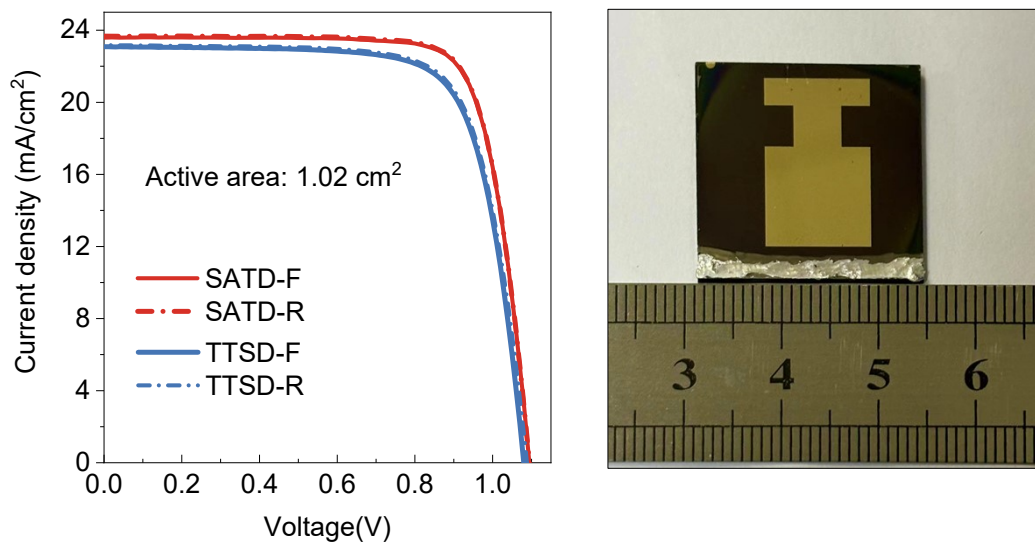
Supplementary Fig. 21. (a) *J–V* curves (under forward and reverse scanning direction) of 2D FA-based PSCs with the active area of 1.02cm^2, based on TTSD and SATD strategy, respectively. (b) and corresponding optical image of device. The main parameters of the best devices are summarized in **Supplementary Table 9**.

Measurement Report

Report No. 24TR082701

Client Name	Shanghai Jiao Tong University
Client Address	800 Dongchuan Road, Minhang, Shanghai, China
Sample	Perovskite solar cell
Manufacturer	Shanghai Jiao Tong University
Measurement Date	27th August, 2024

Performed by:	Qiang Shi	**Date:**	
Reviewed by:	Wenjie Zhao	**Date:**	
Approved by:	Yucheng Liu	**Date:**	27/08/2024

1 / 3

Report No. 24TR082701

==== Measurement Results ====

	Forward Scan (Isc to Voc)	Reverse Scan (Voc to Isc)
Area	101.91 mm^2	
Isc	23.951 mA	23.955 mA
Voc	1.116 V	1.119 V
Pmax	19.869 mW	19.430 mW
Ipm	21.669 mA	21.341 mA
Vpm	0.917 V	0.910 V
FF	74.34 %	72.47 %
Eff	19.50 %	19.07 %

- Spectral Mismatch Factor SMM=0.9980.
- Designated illumination area defined by a thin mask was measured by measuring microscope.
- Test results listed in this measurement report refer exclusively to the mentioned measured sample.
- The results apply only at the time of the test, and do not imply future performance.
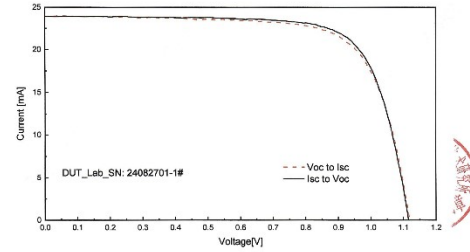
Fig.1 I-V curves of the measured sample

------End of Report------

3 / 3

Supplementary Fig. 22 The certificated I-V curve of the FA-based 2D PSCs, by Shanghai Institute of Microsystem and Information Technology, Chinese Academy of Science (SIMIT).
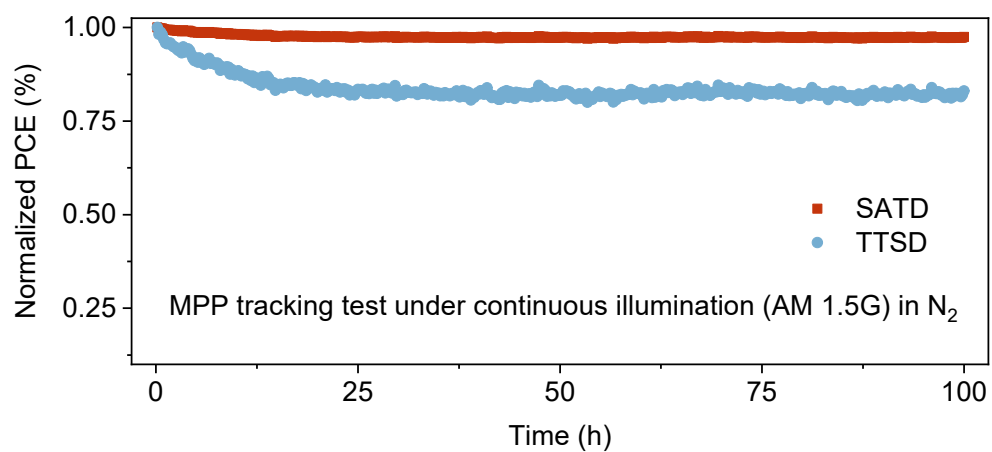
Supplementary Fig. 23. MPP tracking test of the devices based on SATD and TTSD strategy under continuous 1 Sun illumination (AM 1.5G) in N_2, respectively.
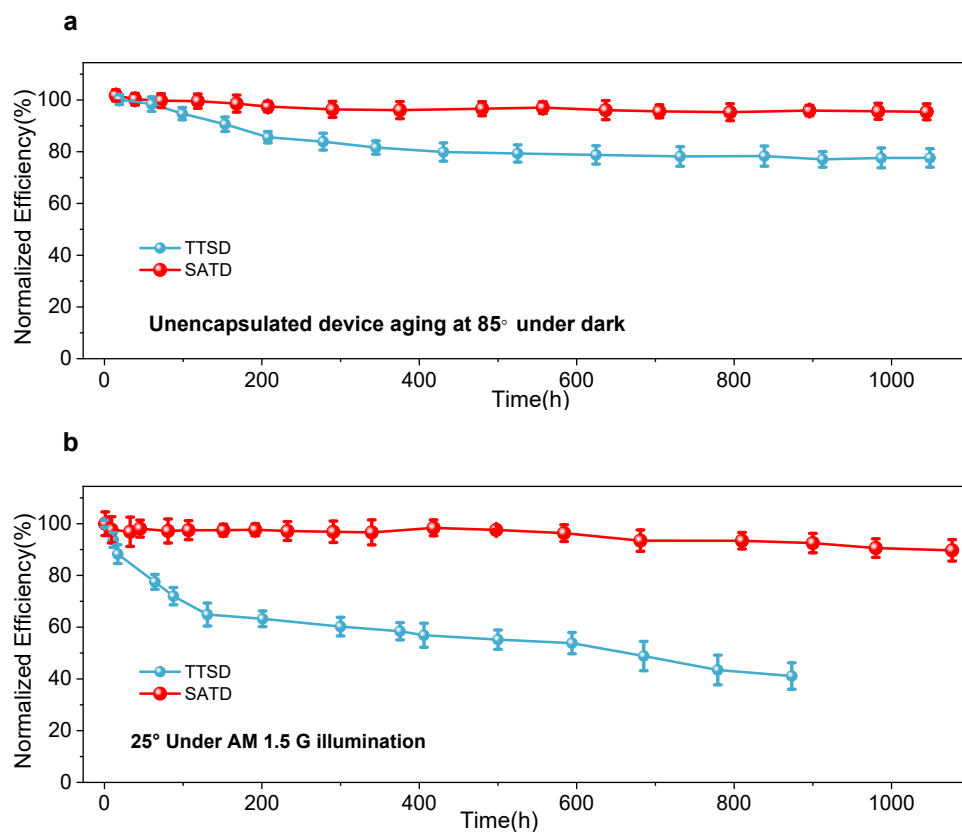
Supplementary Fig. 24. The comparative stability of unencapsulated 2D PSCs employing TTSD and SATD strategy. **a)** Thermal endurance tested at a sustained temperature of 85 °C (dark condition, RH~30±5%), and **b)** Photo-stability of the devices exposed under AM 1.5 G illumination at 25°C.

Supplementary Table 1, The C, H, N and S content of resulted 2D perovskite film $(C_6H_{16}N_1)_2 (CH_5N_2))_{n-1}Pb_nI_{3n+1})$ via Elemental Analysis test.

Mass ratio	N [%]	C [%]	H [%]	S [%]
Sample [1#]	42.6	45.4	12.2	<0.10
Sample [2#]	43.1	44.4	12.0	<0.10
Sample [3#]	43.5	44.7	12.1	<0.10
Average	43.1	44.8	12.1	<0.10
Mole ratio	1.00	1.21	3.90	

Supplementary Table 2. The charge carrier lifetime of the 2D perovskite film based on different spacer cations, such as ThDMA, PEAI, and HAI ($n = 4$) 2D perovskite films, and HA-based 2D perovskite films with different thickness of QWs prepared by the TTSD and SATD strategy.

	TTSD		SATD	
2D PVSK	τ_1 [ns]	τ_2 [ns]	τ_1 [ns]	τ_2 [ns]
HA(n=3)	9.78	89.03	18.37	109.71
HA(n=2)	5.73	47.20	8.45	60.77
ThDMA(n=4)	18.65	144.83	26.35	212.01
PEA(n=4)	9.79	91.58	23.06	153.12
HA(n=4)	6.38	221.41	88.59	932.42

Supplementary Table 3. Main parameters of the best devices of various FA-based 2D perovskites films based on different spacer cations, such as ThDMA, PEAI, and HAI ($n = 4$) 2D perovskite films, and HA-based 2D perovskite films with different thickness of QWs prepared by the TTSD and SATD strategy.

	Methods	V_{oc} (V)	J_{sc} (mA/cm^2)	FF (%)	Efficiency (%)

HA (n=2)	TTSD	1.005	13.05	70.98	9.31
	SATD	1.038	13.39	72.07	10.02
HA (n=3)	TTSD	1.038	18.79	73.59	14.36
	SATD	1.060	20.04	75.03	15.94
PEAI (n=4)	TTSD	1.061	21.77	73.02	16.87
	SATD	1.081	23.16	78.26	19.58
ThDMA (n=4)	TTSD	1.079	22.47	71.97	17.45
	SATD	1.106	22.97	78.18	19.86

Supplementary Table 4. Main parameters (obtained in the forward scanning and reverse scanning) of the best devices of various FA-based 2D perovskites based on the ratio of PbI_2: TU= 1:0.5, 1:1, 1:1.5, 1:2 using SATD strategy, respectively.

Ratio	Direction	V_{oc} (V)	J_{sc} (mA/cm^2)	FF (%)	Efficiency (%)
Control	Forward	1.025	22.49	75.08	17.31
	Reverse	1.021	21.94	78.28	17.53
1:0.5	Forward	1.054	21.97	78.29	18.13
	Reverse	1.066	21.95	78.67	18.41
1:1	Forward	1.126	23.71	79.25	21.16
	Reverse	1.122	23.65	79.05	20.98
1:2	Forward	1.059	22.68	79.66	19.13
	Reverse	1.073	22.65	79.03	19.20

Supplementary Table 5. Main parameters of the best devices of various FA-based 2D perovskites films based on different methods, respectively.

	Direction	V_{oc} (V)	J_{sc} (mA/cm^2)	FF (%)	Efficiency (%)
TTSD	Forward	1.043	21.67	76.60	17.32

	Reverse	1.034	21.69	78.40	17.58
ATSD	Forward	1.081	21.82	79.83	19.06
	Reverse	1.085	21.47	79.55	19.11
STSD	Forward	1.052	21.10	79.77	17.70
	Reverse	1.058	21.23	78.91	17.72
SATD	Forward	1.126	23.71	79.25	21.16

Supplementary Table 6. Summary of the representative low-n 2D PSCs with small areas (< 0.1 cm^2).

Perovskites	n	PCE (%)	J_{sc} (mA/cm^2)	Method	Ref
RP type PSCs					
$BA_2MA_3Pb_4I_{13}$	4	11.10	14.20	Co-solvents	[10]
$BA_2MA_3Pb_4I_{13}$	4	12.52	16.76	Hot casting	[11]
$BA_2MA_3Pb_4I_{13}$	4	13.68	19.94	Cesium doping	[12]
$BA_2MA_3Pb_4I_{13}$	4	17.26	19.86	Annealing	[13]
$BA_2MA_3Pb_4I_{13}$	4	16.25	16.75	Additives	[14]
$BA_2MA_3Pb_4I_{13}$	4	16.48	18.67	Additives	[15]
$BA_2MA_3Pb_4I_{13}$	4	17.10	17.56	Memory seeds	[16]
$(BA)_{1.6}(MA)_{3.4}Pb_4I_{13}$	4	16.29	20.44	Nonpreheating	[17]
$BEA_2MA_3Pb_4I_{13}$	4	16.10	20.63	Spacer cations	[18]
$(3BBA)_{1.8}MA_{2.5}Pb_3I_{10}$	3	18.20	18.22	Hot casting	[19]
$(ThMA)_2MA_2Pb_3I_{10}$	3	15.42	18.89	Additives	[20]
$PEA_2FA_3Pb_4I_{13}$	4	11.30	14.70	Additives	[21]
$PEA_2MA_3Pb_4I_{13}$	4	18.48	18.52	Additives	[22]
$PEA_2MA_3Pb_4I_{13}$	4	17.03	18.47	Additives	[23]
$FPEA_2MA_3Pb_4I_{13}$	4	15.20	13.70	Hydrothermal	[24]
$PEA_{0.2}BA_{1.8}MA_3Pb_4I_{13}$	4	15.81	16.51	Post-treatment	[25]
$(NpMA)_2MA_3Pb_4I_{13}$	4	17.25	20.89	Anti-solvents	[26]
$ThFA_2MA_2Pb_3I_{10}$	3	16.72	20.17	Anti-solvents	[27]
$F-PEA_2MA_3Pb_4I_{13}$	4	18.10	19.04	Additives	[28]
$BA_2FA_3Pb_4I_{13}$	4	18.14	21.62	Additives	[29]
$HA_2FA_3Pb_4I_{13}$	4	20.03	23.60	Additives	[30]
$(BM)(BA)MA_3Pb_4I_{13}$	4	17.30	19.80	Ionic Liquid	[31]
$AA_2MA_3Pb_4I_{13}$	4	18.42	18.57	Post annealing	[32]
$BA_2FA_2Pb_3I_{10}$	3	15.4	15.12	Solvent vapor	[7]
$(DFAz)_2(MA_{0.95}FA_{0.05})_3Pb_4I_{13}$	4	19.85	22.28	Spacer cations	[33]

HA$_2$FA$_3$Pb$_4$I$_{13}$	4	21.16	23.71	SATD	This work
DJ and ACI-type PSCs					
GAMA$_4$Pb$_4$I$_{13}$	4	15.27	20.14	Additives	[34]
(GA)(MA)$_3$Pb$_3$I$_{10}$	3	18.48	22.26	Additives	[35]
GA(MA)$_n$Pb$_n$I$_{3n+1}$	4	18.90	23.10	Interfacial	[36]
BDA$_2$MA$_3$Pb$_4$I$_{13}$	4	14.38	19.90	Additives	[37]
(PDMA)(MA)$_3$Pb$_4$I$_{13}$	4	15.81	21.10	Hot casting	[38]
(MAMP)MA$_3$Pb$_4$I$_{13}$	4	16.53	17.97	Additives	[39]
(3AMP) (MA$_{0.75}$FA$_{0.25}$)$_3$Pb$_4$I$_{13}$	4	18.67	19.51	Annealing	[40]
(3AMP) (MA$_{0.75}$FA$_{0.25}$)$_3$Pb$_4$I$_1$	4	16.25	17.91	Additives	[41]
PDMA$_2$FA$_3$Pb$_4$I$_{13}$	4	7.11	11.48	Space cations	[42]
PDAFA$_3$Pb$_4$I$_{13}$	4	13.80	17.30	Additives	[43]
PDA$_{0.9}$PA$_{0.2}$FA$_3$Pb$_4$I$_{13}$	4	16.00	17.60	Additives	[44]

Supplementary Table 7. The corresponding parameters of each device in the reproducibility measurements.

	TTSD				SATD			
M	V_{oc} (V)	J_{sc} (mA/cm²)	FF (%)	PCE	V_{oc} (V)	J_{sc} (mA/cm²)	FF (%)	PCE (%)
1	1.056	21.44	72.92	16.51	1.126	23.66	78.64	20.95
2	1.037	21.17	76.64	16.82	1.118	23.66	79.11	20.93
3	1.056	21.12	74.83	16.69	1.106	23.30	79.44	20.47
4	1.039	20.84	76.24	16.51	1.119	23.17	79.39	20.58
5	1.021	22.26	74.58	16.95	1.117	23.42	79.35	20.76
6	1.045	21.10	76.83	16.94	1.126	23.70	78.20	20.87
7	1.01	21.53	77.38	16.82	1.121	23.72	78.21	20.80
8	1.068	21.35	74.94	17.09	1.113	23.85	78.59	20.86
9	1.033	21.46	77.42	17.16	1.125	23.76	76.96	20.57
10	1.043	22.21	73.69	17.07	1.128	23.02	79.85	20.73
11	1.02	21.24	77.61	16.82	1.096	23.68	79.80	20.71

12	1.016	21.66	76.46	16.82	1.105	23.49	80.12	20.80
13	1.011	21.72	77.05	16.92	1.106	23.87	78.29	20.67
14	1.033	21.44	76.63	16.98	1.125	23.84	77.12	20.68
15	1.013	21.64	75.31	16.51	1.133	23.6	77.22	20.65
16	0.998	22.14	76.93	17.00	1.122	23.43	79.11	20.80
17	1.001	21.80	79.12	17.27	1.094	23.79	79.85	20.78
18	1.042	21.11	76.93	16.92	1.104	23.61	80.18	20.90
19	1.033	22.13	75.31	17.21	1.110	23.63	79.14	20.76
20	1.041	21.34	76.16	16.92	1.121	23.47	78.23	20.58
21	1.018	22.15	74.62	16.82	1.096	23.58	79.92	20.65
22	1.011	21.93	76.32	16.92	1.117	23.44	78.56	20.57
23	1.054	22.18	73.83	17.26	1.112	23.49	79.01	20.64
24	1.021	21.73	79.17	17.57	1.079	23.69	80.11	20.48
25	1.012	22.35	76.21	17.24	1.112	23.15	80.20	20.65
26	1.044	21.78	75.23	17.11	1.117	23.26	79.17	20.57
27	1.038	21.77	76.20	17.22	1.116	23.35	80.04	20.86
28	1.041	22.13	76.28	17.57	1.135	23.69	76.59	20.59
29	1.034	21.75	76.14	17.12	1.113	23.49	79.18	20.70
30	1.042	21.59	76.23	17.15	1.128	23.53	78.15	20.74

Supplementary Table 8. Main parameters (obtained in the forward scanning and reverse scanning) of the best devices based on traditional one-step method of adding TU and SATD methods.

	Direction	V_{oc} (V)	J_{sc} (mA/cm^2)	FF (%)	Efficiency (%)
One-step Method	Forward	1.084	23.12	79.49	19.93
	Reverse	1.072	23.05	79.03	19.53
SATD	Forward	1.126	23.71	79.25	21.16
	Reverse	1.122	23.65	79.05	20.98

Supplementary Table 9. Main parameters (obtained in the forward scanning and reverse scanning) of the best devices of various FA-based 2D perovskite films at the active area of 1.02cm^2.

	Direction	V_{oc} (V)	J_{sc} (mA/cm^2)	FF (%)	Efficiency (%)
TTSD	Forward	1.080	22.64	74.09	18.11
	Reverse	1.088	22.71	74.17	18.33
SATD	Forward	1.094	23.53	77.67	20.00
	Reverse	1.095	23.47	77.74	19.99

Supplementary Table 10. Summary of the representative 2D PSCs with large areas ($\geq$ 1cm^2).

Perovskites	n[a]	Types	Areas (cm^2)	PCE (%)	Ref
$BA_2MA_3Pb_4I_{13}$	4	RP	1	14.81	[45]
$BA_2MA_3Pb_4I_{13}$	4	RP	16	11.13	[45]
$HA_2FA_3Pb_4I_{13}$	4	RP	1	18.70	[1]
$(4FPEA)_2(FA)_4Pb_5I_{16}$	5	RP	1	18.40	[46]
$GAMA_5Pb_5I_{16}$	5	ACI	1	19.08	[47]
$GAMA_5Pb_5I_{16}$	5	ACI	1.01	19.68	[48]
$GAMA_5Pb_5I_{16}$	5	ACI	65.7	14.70	[48]
$HA_2FA_3Pb_4I_{13}$	4	RP	1.02	20.00	This work

[a] Designated layer thickness of QWs.

Supplementary Table 11. The initial average PCE of the devices for stability tests using PTAA as HTL.

	Stability	V_{oc} (V)	J_{sc} (mA/cm^2)	FF (%)	Efficiency (%)
Initial PCE	Humid	1.10	23.69	79.80	20.79
	Thermal	1.11	23.64	78.89	20.70
	Light	1.10	23.61	77.73	20.19

Supplementary References

1   Zeng, F. *et al.* Highly stable and efficient formamidinium-based 2D Ruddlesden–Popper perovskite solar cells via manipulation. *Advanced Materials* **35**, 2306051 (2023).

2   Kohn, W. *et al.* Self-consistent equations including exchange and correlation effects. *Physical Review* **140**, A1133 (1965).

3   Kresse, G. *et al.* Efficiency of ab-initio total energy calculations for metals and semiconductors using a plane-wave basis set. *Computational materials science* **6**, 15-50 (1996).

4   Grimme, S. *et al.* A consistent and accurate ab initio parametrization of density functional dispersion correction (DFT-D) for the 94 elements H-Pu. *The Journal of Chemical Physics* **132** (2010).

5   Kresse, G. *et al.* From ultrasoft pseudopotentials to the projector augmented-wave method. *Physical review b* **59**, 1758 (1999).

6   Perdew, J. P. *et al.* Generalized gradient approximation made simple. *Physical review letters* **77**, 3865 (1996).

7   Chen, B. *et al.* Surface crystallization modulation toward highly-oriented and phase-pure 2D perovskite solar cells. *Advanced Materials* **36**, 2312054 (2024).

8   Paritmongkol, W. *et al.* Synthetic variation and structural trends in layered two-dimensional alkylammonium lead halide perovskites. *Chemistry of Materials* **31**, 5592-5607 (2019).

9   Lai, H. *et al.* Organic-salt-assisted crystal growth and orientation of quasi-2D Ruddlesden–Popper perovskites for solar cells with efficiency over 19%. *Advanced Materials* **32**, 2001470 (2020).

10   Caiazzo, A. *et al.* Effect of co-solvents on the crystallization and phase Distribution of Mixed-Dimensional Perovskites. *Advanced Energy Materials* **11**, (2021).

11   Tsai, H. *et al.* High-efficiency two-dimensional Ruddlesden–Popper perovskite solar cells. *Nature* **536**, 312-316, (2016).

12   Zhang, X. *et al.* Stable high-efficiency two-dimensional perovskite solar cells via cesium doping. *Energy & Environmental Science* **10**, 2095-2102, (2017).

13   Wu, G. *et al.* Fine Multi-Phase Alignments in 2D Perovskite Solar Cells with Efficiency over 17% via Slow Post-Annealing. *Advanced Materials* **31**, (2019).

14   Liang, C. *et al.* Two-dimensional Ruddlesden-Popper layered perovskite solar cells based on phase-pure thin films. *Nature Energy* **6**, 38-45, (2021).

15   Song, J. *et al.* Unraveling the crystallization kinetics of 2D perovskites with sandwich-type structure for high-performance photovoltaics. *Advanced Materials* **32**, 202002784 (2020).

16   Sidhik, S. *et al.* Memory seeds enable high structural phase purity in 2D perovskite films for high-efficiency devices. *Advanced Materials* **33**, (2021).

17   Li, X. *et al.* Non-preheating processed quasi-2D perovskites for efficient and stable solar cells. *Small* **16**, (2020).

18   Chao, L. *et al.* Efficient and stable low-dimensional Ruddlesden-Popper

perovskite solar cells enabled by reducing tunnel barrier. *Journal of Physical Chemistry Letters* **10**, 1173-1179, (2019).

19   Yang, R. *et al.* Oriented quasi-2D perovskites for high-performance optoelectronic devices. *Advanced Materials* **30**, (2018).

20   Lai, H. *et al.* Two-dimensional Ruddlesden-Popper perovskite with nanorod-like morphology for solar cells with efficiency exceeding 15%. *Journal of the American Chemical Society* **140**, 11639-11646, (2018).

21   Qing, J. *et al.* Aligned and graded type-II Ruddlesden–Popper perovskite films for efficient solar cells. *Advanced Energy Materials* **8**, 1800185, (2018).

22   Yang, Y. *et al.* Defect suppression in oriented 2D perovskite solar cells with efficiency over 18% via rerouting crystallization Pathway. *Advanced Energy Materials* **11**, (2021).

23   Yang, Y. *et al.* Universal approach toward high-efficiency two-dimensional perovskite solar cells via a vertical-rotation process. *Energy & Environmental Science* **13**, 3093-3101, (2020).

24   Liang, J. *et al.* Overcoming the carrier transport limitation in Ruddlesden-Popper perovskite films by using lamellar nickel oxide substrates. *Journal of Materials Chemistry A* **9**, 11741-11752, (2021).

25   Lian, X. *et al.* Two-dimensional perovskite solar cells with high luminescence and ultra-low open-circuit voltage deficit. *Journal of Materials Chemistry A* **8**, 22175-22180, (2020).

26   Xu, Z. *et al.* Phase distribution and carrier dynamics in multiple-ring aromatic spacer-based two-dimensional Ruddlesden-Popper perovskite solar cells. *Acs Nano* **14**, 4871-4881, (2020).

27   Dong, Y. *et al.* 2-Thiopheneformamidinium-Based 2D Ruddlesden-Popper perovskite solar cells with an efficiency of 16.72% and negligible hysteresis. *Advanced Energy Materials* **10**, (2020).

28   Wang, Z. *et al.* Spacer cation tuning enables vertically oriented and graded quasi-2D perovskites for efficient solar cells. *Advanced Functional Materials* **31**, (2021).

29   Kong, W. *et al.* Oriented low-n Ruddlesden-Popper formamidinium-based perovskite for efficient and air-stable solar cells. *Advanced Energy Materials* **12**, (2022).

30   Zeng, F. *et al.* Highly stable and efficient formamidinium-based 2D Ruddlesden-Popper perovskite solar cells via lattice manipulation. *Advanced Materials* **35**, (2023).

31   Liu, C. *et al.* Imidazolium ionic liquid as an organic spacer for tuning the excitonic structure of 2D perovskite materials. *ACS Energy Letters* **5**, 3617-3627, (2020).

32   Wu, G. *et al.* Molecular engineering for two-dimensional perovskites with photovoltaic efficiency exceeding 18%. *Matter* **4**, (2021).

33   Blancon, J. C. *et al.* Scaling law for excitons in 2D perovskite quantum wells. *Nature Communications* **9**, 2254, (2018).

34   Zhang, Y. *et al.* Highly efficient guanidinium-based quasi 2D perovskite solar

cells via a two-step post-treatment process. *Small Methods* **3**, (2019).

35   Luo, T. *et al.* Compositional Control in 2D Perovskites with Alternating Cations in the Interlayer Space for Photovoltaics with Efficiency over 18%. *Advanced Materials* **31**, (2019).

36   Wang, H., Yang, F., Li, X. & Zhang, P. Fully Printed High-Performance Quasi-Two-Dimensional Perovskite Solar Cells via Multifunctional Interfacial Engineering. *Advanced Functional Materials* **34**, 2312250 (2024).

37   Zhang, Y. *et al.* Effective Phase-Alignment for 2D Halide Perovskites Incorporating Symmetric Diammonium Ion for Photovoltaics. *Advanced Science* **8**, (2021).

38   Zhang, X. *et al.* Film Formation Control for High-Performance Dion-Jacobson 2D Perovskite Solar Cells. *Advanced Energy Materials* **11**, (2021).

39   He, T. *et al.* Reduced-dimensional perovskite photovoltaics with homogeneous energy landscape. *Nature Communications* **11**, (2020).

40   Wu, H. *et al.* Merged interface construction toward ultra-low V-oc loss in inverted two-dimensional Dion-Jacobson perovskite solar cells with an efficiency of over 18%. *Journal of Materials Chemistry A* **9**, 12566-12573, (2021).

41   Wu, H. *et al.* in *47th IEEE Photovoltaic Specialists Conference (PVSC).*   93-95 (2020).

42   Li, Y. *et al.* Bifunctional Organic Spacers for Formamidinium-Based Hybrid Dion-Jacobson Two-Dimensional Perovskite Solar Cells. *Nano Letters* **19**, 150-157, (2019).

43   Cheng, L. *et al.* Highly Thermostable and Efficient Formamidinium-Based Low-Dimensional Perovskite Solar Cells. *Angewandte Chemie-International Edition* **60**, 856-864, (2021).

44   Cheng, L. *et al.* Tailoring Interlayer Spacers for Efficient and Stable Formamidinium-Based Low-Dimensional Perovskite Solar Cells. *Advanced Materials* **34**, (2022).

45   Han, C. *et al.* Tailoring Phase Alignment and Interfaces via Polyelectrolyte Anchoring Enables Large-Area 2D Perovskite Solar Cells. *Angewandte Chemie* **134**, e202205111 (2022).

46   Shao, M. *et al.* Over 21% efficiency stable 2D perovskite solar cells. *Advanced Materials* **34**, 2107211 (2022).

47   Xu, C. *et al.* Fast Solidification and Slow Growth Strategy for High-Performance Quasi-2D Perovskite Solar Cells. *Advanced Energy Materials* **13**, 2300168 (2023).

48   Xing, Z. *et al.* Repairing Humidity-Induced Interfacial Degradation in Quasi-2D Perovskite Solar Cells Printed in Ambient Air. *Energy & Environmental Science* (2024).